

Cold Gas Simulations of the Influence of Inhibitor Shape in Combustor Combustion

Jérôme Vétel,* Frédéric Plourde,[†] and Son Doan-Kim[‡]

*Laboratoire d'Etude Thermique/Ecole Nationale Supérieure de Mécanique et d'Aérotechnique,
86960 Futuroscope Cedex, France*

and

Michel Prevost[§]

ONERA, 31410 Mauguac, France

A cold-gas setup is used to analyze the internal acoustic response of small-scale solid propellant rocket motors. These motors are characterized by a forward, a central, and an aft segment, with nonablative inhibitors on the last segment forward face. Investigations have been carried out with four inhibitors with different protrusions and shapes, each leading to specific pressure oscillation behavior. The cold-flow setup has been designed to reproduce the general features of the internal geometry of the combustors corresponding to two burning times. It is found that pressure measurements reproduce the acoustic response of firing tests with satisfactory agreement. Velocity fluctuations are used to analyze vortex-shedding-driven pressure oscillations. Measurements in the shear layer generated downstream from the inhibitors and in the vicinity of the injecting wall allow identification of the development of two vortex fields. Experiments with small inhibitors show the development of only one kind of instability, combining the vortex development of the shear layer with an effect of vorticity amplification due to the wall injection. Finally, an estimation of the convection velocity is proposed to explain resonance frequency evolution during the combustion.

I. Introduction

COLD-FLOW experiments are extensively used to simulate the internal unsteady behavior of solid rocket motors. During combustion, a large number of phenomena can develop and change the stability of the motor that may affect its firing. More specifically, cold-gas simulations represent an easy and useful step in analysis of the vortex-shedding responsible for acoustic pressure oscillations. This mechanism was first expected to occur from protruding inhibitors placed in the flow, used for the insulation of the propellant segment end faces. A large number of studies have described the coupling mechanism between the vortex-shedding formation behind the inhibitor and pressure oscillations through experiments conducted in duct flows with baffles.^{1–4} The basic phenomenon is linked to an acoustic feedback resulting from impingement of vortices upon an obstacle. Numerous demonstrated examples are available in the literature dealing with cavity tone, hole tone, edge tone, or ring tone,^{5,6} and some similarities may be found with the internal configuration of segmented solid propellant rocket motors, where the acoustic feedback results from impingement of vortices upon the nozzle. Other works have been dedicated to the characterization of flows generated by wall injection by using porous walls to simulate the internal aerodynamic. The mean flowfield and turbulence development^{7,8} were investigated, as well as the effects induced by the use of porous material.⁹ The analysis of mean and fluctuating

velocities in a simulated cylindrical port rocket chamber by Dunlap et al.¹⁰ was of major importance and led to the first observation of vortices close to the injecting wall.

Since the first experiments devoted to the simulation of solid rocket motors, improvement of computer performance has given new impetus to the understanding of flows developing in combustion chambers. The use of a time-dependent two-equation model by Shu et al.¹¹ and the numerical simulation in a two-dimensional case of Menon and Jou¹² are some examples of the first approaches in this field. Later, Lupoglazoff and Vuillot¹³ confirmed numerically the existence of the wall vortices and they were the first to consider the coupling with the acoustic as a driven mechanism. Thanks to large-eddy simulation,^{14,15} the turbulence effects are better taken into account but require a subgrid-scale turbulence model in a position to take into account the complex geometry and all of the dynamic scales of these particular flows, including the unknown scales introduced by the injecting wall. Moreover, the numerical calculations are mainly restricted to one burning time. In computation of the unstable flow behavior during a whole firing, a varying burning rate surface module has to be coupled with the simulations of the fluid dynamic.¹⁶ However, such simulations are conducted with simplifications and generally for a two-dimensional case. That is the reason why cold-gas experiments are useful, not only for numerical validation but also from a fundamental point of view. The cold-gas setup used here is dedicated to this approach and is both sufficiently representative to exhibit the elementary phenomena that are supposed to occur in a three-segmented motor and basic enough to allow for appropriate analysis of the characteristics of the fluctuating flowfield. In spite of a non-symmetric two-dimensional configuration, which could seem restrictive, the cold flow setup has been built to reproduce the general features of the aerodynamic of small rocket motors, including the propellant segments, the inhibitors, and a nozzle in the rear end.

The aim of this study is to analyze pressure oscillations occurring in four combustors with inhibitors that exhibit different shapes and protrusions in the flow. The acoustic responses of the firing tests are first compared with the results from cold-gas experiments. After that, a complete investigation of the flow field by velocity fluctuation analyses provide, as deduced from previous fundamental works, a full understanding of the occurrence of vortex-shedding-driven pressure oscillations.

Presented as Paper 2003-9605 at the AIAA/ASME/SAE/ASEE Joint Propulsion Conference and Exhibit, Huntsville, AL, 20–23 July 2003; received 6 January 2004; revision received 12 July 2004; accepted for publication 30 July 2004. Copyright © 2004 by the American Institute of Aeronautics and Astronautics, Inc. All rights reserved. Copies of this paper may be made for personal or internal use, on condition that the copier pay the \$10.00 per-copy fee to the Copyright Clearance Center, Inc., 222 Rosewood Drive, Danvers, MA 01923; include the code 0748-4658/05 \$10.00 in correspondence with the CCC.

*Postdoctoral Researcher, LET/ENSMA, Téléport 2, 1 Avenue Clément Ader, BP 109. Student Member AIAA.

[†]Senior Scientist, Centre National de la Recherche Scientifique, (LET/ENSMA UMR 6607), Téléport 2, 1 Avenue Clément Ader, BP 109. Member AIAA.

[‡]Professor, University of Poitiers, Téléport 2, 1 Avenue Clément Ader, BP 109.

[§]Scientist, ONERA/DMAE, Centre du Fauga–Mauguac.

II. Experimental Investigations

A. Small-Scale Motors and Definition of Test Cases


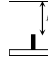

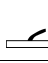
The combustors studied are subscale motors of the solid rocket motors of Ariane 5. The propellant is a nonmetallized propellant containing nonactive stabilizing additives. The geometry, given in Fig. 1, shows the presence of conical propellant grains in both central and aft segments, as well as a head-end star-shaped grain. A thermal protection is placed at the first intersegment, whereas the aft segment forward face is insulated with a metallic inhibitor. The use of the latter was naturally motivated by its nonablativ property so that the diameter of the section is known whatever the combustion time and because any possible coupling between the flow oscillations and the vibration of the inhibitor is excluded because it has been replaced by a rigid metallic part. A detailed description of the experimental configuration and data reduction is given in Ref. 17.

Among the combustor configurations available, investigations were performed on motors that present similar propellant segments and four kind of inhibitors, as presented in Table 1. The first configuration (test case 1) is characterized by a straight inhibitor that strongly reduces the internal section between the two propellant segments. The second test case involves a straight inhibitor, whose height is lower than the first one. The height of the inhibitor in the third configuration is the same as the second one, but its shape is

curved. Finally, the last test case presents an inhibitor with a strong bent shape and small section reduction.

The changes in pressure oscillation spectra during the combustion time are presented in Fig. 2. For test case 1, weak oscillations occur for $3 < t < 6$ s on the third acoustic mode. The second test case shows first pressure organization on the third mode, then the second, and finally the first acoustic mode at approximately 9 s, that is, at the end of the combustion. Pressure oscillations are observed

Table 1 Presentation of test cases

Test case	Geometry of the inhibitor	Characteristic length ℓ , mm	Mass flow rate ratio α_q ($t = t_2$)
1		16	0.43
2		26	0.43
3		26	0.46
4		30	0.44

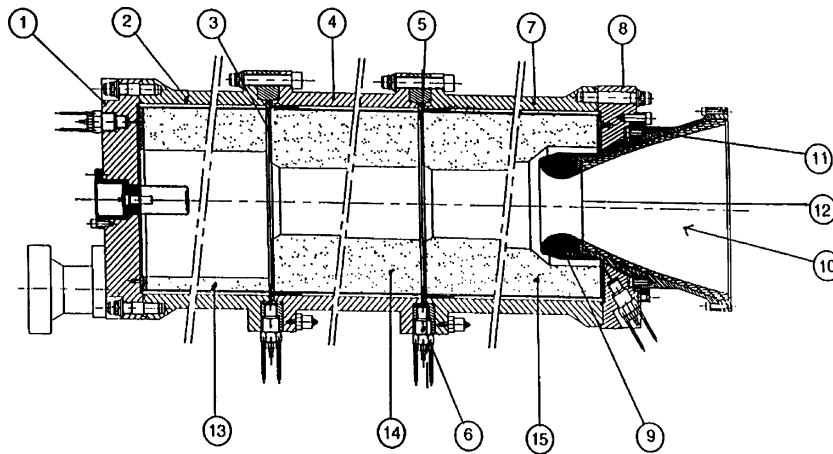


Fig. 1 Combustor: 1) head-end closure with igniter, 2) forward case, 3) intersegment 1, 4) central case, 5) intersegment 2, 6) pressure transducer, 7) aft case, 8) aft-end closure, 9) nozzle throat, 10) nozzle, 11) divergent part of the nozzle, 12) seal cap, 13) first propellant segment, 14) second propellant segment, and 15) third propellant segment.

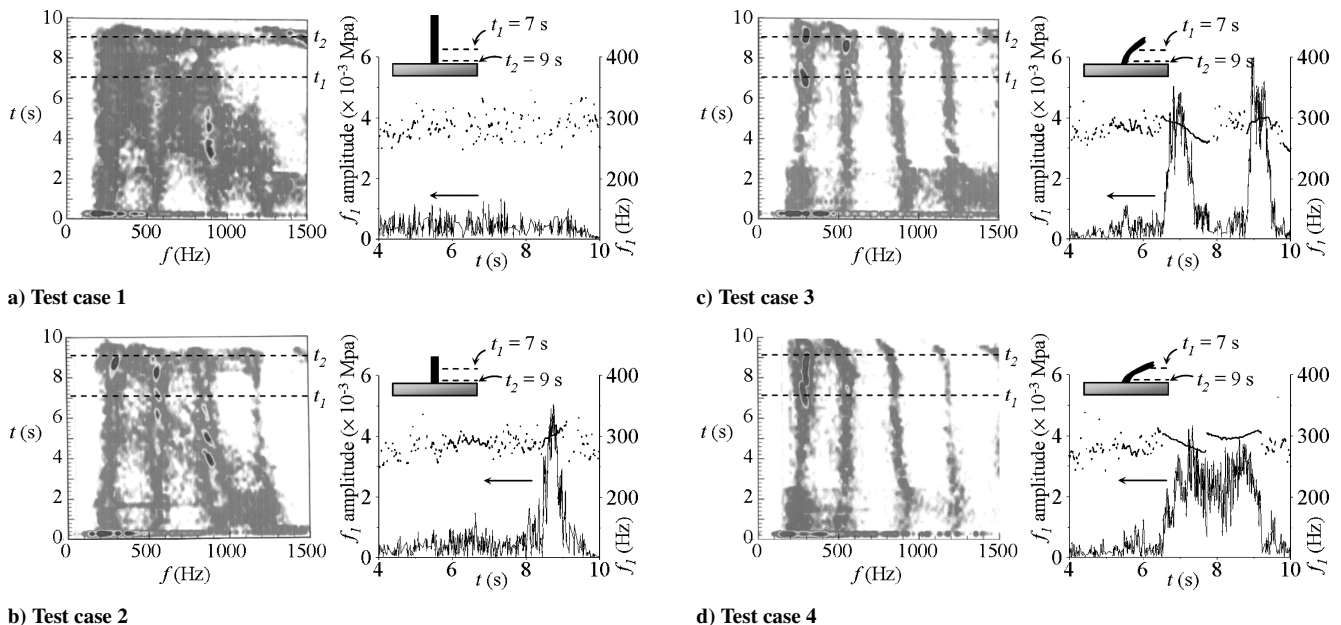


Fig. 2 Acoustic responses of test cases and time evolutions of first acoustic mode.

only for $t > 6$ s for test case 3, involving to some extent the second mode, but mainly the first mode. For the last configuration, a strong amplification of the first mode characterizes the pressure spectra for $6.5 < t < 9$ s.

Because amplifications of oscillations occur mainly at the end of the life of the combustors on a frequency close to the first acoustic mode of the chamber, only instabilities appearing for relatively large combustion times were investigated. The frequency and amplitude of the first longitudinal acoustic mode f_1 are also in Fig. 2. No pressure oscillations have been observed for the first test case, whereas the second one shows a strong amplification around $t = 8.7$ s. Similar behavior is observed for test case 3 at $t \approx t_2 = 9$ s with another amplification occurring at approximately $t_1 = 7$ s associated with a decrease in the frequency. The last configuration studied (test case 4) provides the largest instability duration on the first longitudinal mode ($6.5 < t < 9.2$ s), involving two characteristic evolutions of the first acoustic mode frequency separated by a frequency jump. Thus, cold-gas simulations were chosen to reproduce two combustion times, that is, at $t_1 = 7$ s and $t_2 = 9$ s.

B. Cold-Gas Setup

The cold-flow setup is a model of the combustor with a geometric scaling factor of 2.66. However, the scale model does not completely reproduce the motor but is roughly similar through the presence of three nonconical injecting blocks, simulating the three segments. The flow is generated by injecting air at ambient temperature from a feeding unit. Injection into the channel is performed through a porous wall characterized by a sintered-bronze sphere Poral plate with $2 \mu\text{m}$ characteristic diameter. A submerged nozzle without a cavity is located at the rear end of the chamber to ensure sonic conditions, and the height of the throat can be varied, thereby controlling the mean flow velocity in the chamber. Each intersegment is reproduced as well, with an obstacle providing a scaling of the inhibitor, whose protrusions are shown in Table 1. Hot-wire anemometers and Kistler pressure transducers are used to monitor the oscillations of the flow. A full description of the test channel, measuring techniques, and operating conditions may be found in Refs. 18 and 19.

With use of a monodimensional code,²⁰ the experimental mean pressure inside a combustor is used to obtain the properties of the flow. For each burning time, the internal geometry is estimated and the mass flow rate of the propellant grains is deduced, so that all of the stationary properties of the flow are known. The cold-flow setup was used for two channel heights, $H_c = H_1 = 31$ mm and $H_c = H_2 = 36$ mm, corresponding to the simulations of the combustors for the two combustion times. For these characteristic times, the head-end star-shaped grain is completely burnt, and it is assumed that there is no influence of the second segment thermal protection. At $t = t_1$, 75% of the propellant is burnt and the mass flow rates of the second and the third segments are similar so that cold-gas experiments are used with the same injection velocity for the two injecting blocks. On the contrary, 95% of the propellant is burnt at time $t = t_2$, where the third propellant grain is almost completely burnt, and a sharp decrease of the mean pressure inside the combustors provided by the conicity of the segments is observed. The internal shape of this segment is actually conical so that its length is largely reduced. Thus, two boundary conditions were considered for cold-gas simulations where the injecting area was conserved. The first one allows the conservation of the ratio α_q between the mass flow rate of the third block and that of the second block (Table 1), so that the injection velocity of the third injecting block was reduced to compensate the injection area. For the second boundary condition, the mass flow rate ratio is not conserved, but the cold-gas simulations have been investigated with respect to the mass flow rate per unit area. For this last case, the ratio α_v between the injection velocities of the injecting blocks has been conserved.

The basic phenomena studied with this setup are related to vortex-shedding-driven pressure oscillations from instabilities at inhibitors. The characteristic parameters of the instability are determined by the Strouhal number Sr defined with the momentum thickness θ

(see Ref. 21),

$$Sr = f\theta/U \quad (1)$$

where f is the vortex-shedding frequency and U is the jet exit velocity. By the estimating of the momentum thickness from the calculation of the axial velocity distribution obtained with a transient flow analysis, the study of Wu and Kung²² led to accurate prediction of the acoustic responses of several solid rocket motors exhibiting different types of behaviors. However, in practice, θ cannot be measured. Thus, the Strouhal number is usually based on a characteristic length scale: channel height for planar flows and radius for axisymmetric flows. Moreover, in the event of a coupling phenomenon between vortex shedding and acoustics, the vortex emission frequency corresponds to a longitudinal acoustic mode frequency:

$$f_n = na/2L \quad (2)$$

where a is the speed of sound and L the total length of the chamber. Therefore, the Strouhal number, based on the characteristic length h , is expressed as follows:

$$Sr = (n/2)[(h/L)/M_i] \quad (3)$$

where M_i is the Mach number in the inhibitor section. Thus, the similitude of the unsteady flow between the solid rocket motors and the cold-flow simulations is achieved by scaling the Mach number at the inhibitor location. Contrary to the firing tests, cold-gas simulations are performed for a fixed geometry, but flow behavior is investigated for a Mach number range around the similitude Mach number. Indeed, this allows for analysis of the natural or forced character of oscillations and for the identification of instability frequency evolution and, therefore, the frequency shifts occurring when a coupling phenomenon is observed. In the presentation of the results that follows, the influence of the Mach number M on the unsteady flow is studied. Mach number M value is based on the total mass flow rate injected through the two injecting blocks and the section of the channel. The characteristic Mach number M_c is the value of M for which the similitude with the mean Mach number in the section of the inhibitor is obtained. The first test case was not directly simulated because of the too large value of characteristic Mach number M_c , but is of great importance because it presents the different vortex-shedding phenomena appearing in cold-gas experiments.

III. Cold-Gas Simulations

A. Overview of Vortex-Shedding Phenomena: Test Case 1

Cold-gas results for $H_c = H_1$ are presented in Fig. 3 for the first test case. Figure 3a shows the evolution of the pressure spectra with the available Mach number range. The excitation of the first acoustic mode f_1 is observed for $M < 0.1$ and then a transition to the second mode f_2 occurs. Spectra of velocity fluctuations measured close to the injecting wall are plotted in Fig. 3b. As can be seen, a large frequency range is excited and the increase of the Mach number induces a linear shift of the frequency band. The characteristic shape observed in velocity spectra was found to represent the frequencies involved by a wall vortex development. In a geometric configuration with $H_c = 28$ mm (Ref. 18), wall vortices are shed in a location close to the rear end of the chamber. The presence of an obstacle between the two injecting blocks induces a high level of velocity fluctuations downstream. This effect, combined with the pseudoturbulence injected by the porous wall, strongly affects the wall vortex-shedding frequency at separation and moreover induces an oscillation of the shedding location. Therefore, the vortex passage frequency oscillates in a large range around a central frequency, which explains the spectrum shape. All of these effects were also found to weaken pronouncedly the influence of acoustic velocity oscillations on the vortex-shedding frequencies. In this way, the involved frequencies increase with the Mach number because natural instability and the pressure oscillations generated by vortex–nozzle interaction are responsible for the successive excitation of the acoustic modes of the chamber. The results of Fig. 3 are, therefore, an illustration of wall vortex-shedding-driven resonance mechanisms.

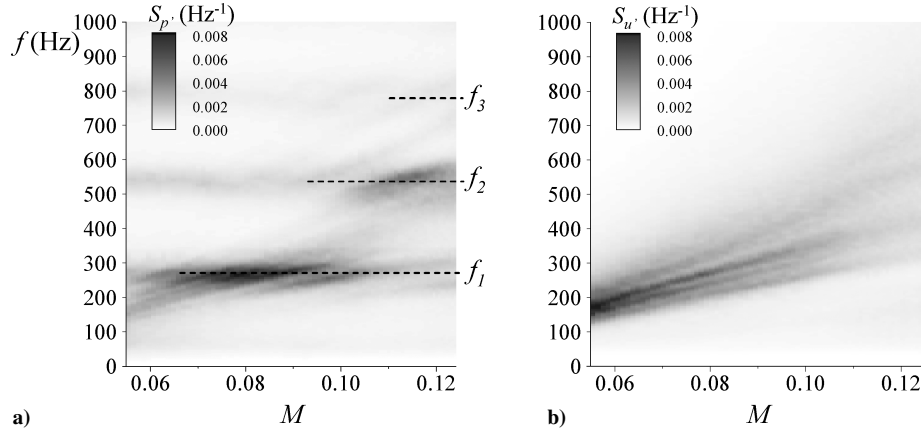


Fig. 3 Cold-gas experiments, test case 1 for $H_c = H_1$: a) pressure spectra and b) wall velocity spectra.

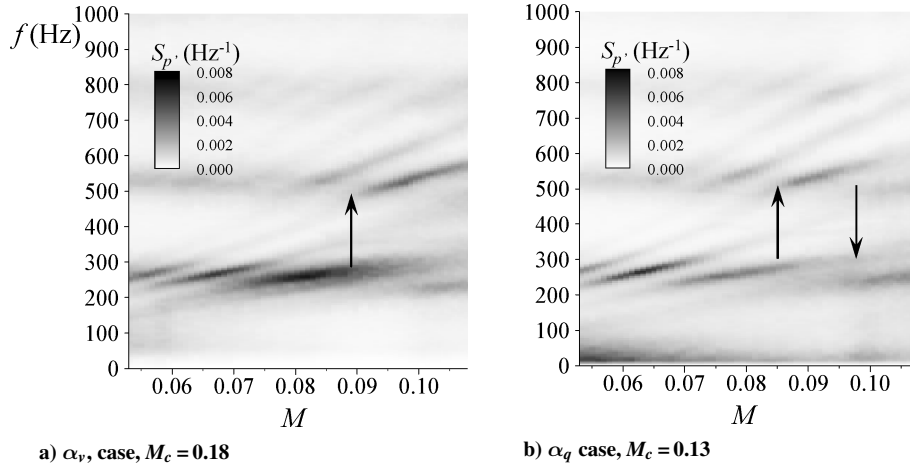


Fig. 4 Pressure spectra of test case 1, cold-gas experiments for $H_c = H_2$.

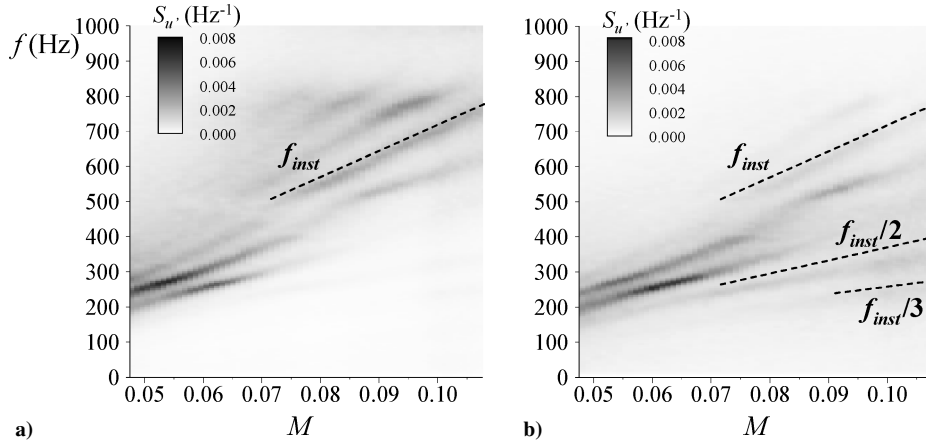


Fig. 5 Shear-layer velocity spectra of test case 1 cold-gas simulation for $H_c = H_2$: a) close to the obstacle location and b) rear end of the chamber.

Figure 4 shows the results obtained for the simulation of the channel height $H_c = H_2$. For the α_v case, shifts of the f_1 frequency are observed for $M < 0.1$ and of the f_2 frequency for $M > 0.08$. When the mass flow rate ratio is conserved, α_q , the pressure oscillation behavior is mainly similar to that of the α_v case. Frequency shifts are observed around the f_1 mode for $M < 0.09$ and close to the second mode for $M > 0.07$. However, an interesting feature arises in the α_q case because, for $M > 0.1$, transition from the second to the first acoustic mode is observed. Additional studies were performed to explain such a mechanism involving the transition from

a given mode to a lower mode despite the increase of the Mach number.

In a previous work,¹⁹ it was shown that in addition to the wall vortex shedding, vortex shedding occurs in the shear layer developing downstream from the top of the obstacle. In the case of an unbalanced mass flow rate between the two injecting blocks, formation of the wall vortices is delayed in the rear end of the chamber. For a relatively large increase of the second injecting block mass flow rate, the shear layer instability is able to drive completely the pressure oscillation behavior. Here, the ratio α_q is close to 0.43 so that no

wall vortices were observed. Under these conditions, Fig. 5 shows spectra of velocity fluctuations recorded for two locations at the upper limit of the shear layer. Close to the obstacle location (Fig. 5a), velocity fluctuations are organized around the first acoustic mode for $M < 0.07$. For higher Mach numbers, several frequency shifts are observed for $f = 500\text{--}800$ Hz. The evolution of the dominant frequency is also plotted, showing a linear evolution with Mach number M , characterizing the occurrence of a natural instability, as observed for the $H_c = 28$ mm configuration.²³ Farther from the obstacle location (Fig. 5b), similar behavior is observed for $M < 0.07$. However, for $M > 0.07$, the excitation of high frequencies is pronouncedly weakened, whereas the fluctuation organization appears around the first mode. In particular, two frequency shifts close to the $f_{\text{inst}}/2$ and $f_{\text{inst}}/3$ frequencies are observed. A vortex pairing mechanism involving the merging of two or three vortices occurs between separation and impingement.¹⁹

The shear layer instability development can, therefore, be described as follows. For lower Mach numbers, the natural vortex-shedding frequency is close to the first acoustic mode and a coupling phenomenon with pressure oscillations generated by vortex impingement on the nozzle is observed. For higher Mach numbers, the vortex-shedding frequency increases and induces excitation of the second acoustic mode. For an additional increase of the Mach number, the vortex-shedding frequency comes to resemble a harmonic of the first acoustic mode. The initial shear layer development is modulated by the acoustic velocity oscillations implying a pairing process. The frequency, then divided by two or three by the merging of two or three vortices, induces shifts around the first acoustic mode. Because no vortex shedding develops in the vicinity of the injecting wall at frequencies close to the second acoustic mode, the shear layer drives the pressure oscillations and induces the transition from the second to the first acoustic mode. In this case, the shear layer vortex shedding is the mechanism driving pressure oscillations. Nevertheless, the high-velocity fluctuations induced by the strongly protruding obstacle disturb the flow, which may explain the absence of instability in firing test case 1.

B. Test Case 2 and Test Case 3

The cold-gas simulations of the second and third firing tests were studied simultaneously, because test case 2 uses a straight inhibitor with the same protrusion in the flow as the curved one in test case 3. Therefore, comparison between the results of these two configurations may be applied to the influence of inhibitor bending. Furthermore, even if the two test cases show instabilities at $t = t_2$, only test case 3 develops pressure oscillations at time $t = t_1$. The pressure spectra obtained for $H_c = H_1$ are shown in Fig. 6. For test case 2, a large frequency band is excited at low Mach numbers. When Mach number M increases, the velocity fluctuations organize on several thin peaks the frequencies of which increase linearly. A coupling phenomenon is, therefore, observed, but for $M > 0.11$, the frequency shifts weaken and the excitation of the second acoustic

mode is observed. However, no discrete frequencies emerge around f_2 ; instead, a large frequency band appears. Different behavior is obtained for test case 3. Even for small Mach numbers, pressure oscillation spectra highlight the presence of discrete frequencies. With the increase of Mach number M , several shifts of the f_1 mode are clearly observed, whereas the excitation of the second mode does not appear. For the two test cases, the characteristic Mach number is $M_c = 0.093$. As seen in Fig. 2, firing test 2 shows at $t = t_1$ only a weak excitation of the second acoustic mode, whereas the pressure oscillations develop with a high level on the first acoustic mode for firing test 3. When a Mach number range around M_c is considered, a satisfactory agreement is obtained between firing tests and cold-gas results.

To analyze in more detail the differences observed between the two simulations, Fig. 7 shows the spectra of velocity fluctuations recorded close to the injecting wall. For test case 2, spectrum behavior is similar to that observed in Fig. 3b, showing the presence of wall vortex development. In addition and as earlier observed in pressure oscillation spectra (cf., Fig. 6), several frequency shifts occur around the first acoustic mode when increasing the Mach number. The results obtained for test case 3 are clearly different. The velocity oscillation frequencies correspond to the pressure fluctuations. This specific behavior is explained by a differing instability mechanism whose origin is linked to the effect of the injected flow on shear layer development.²⁴ Particularly, it was shown that for this kind of configuration, the obstacle induces relatively small perturbations on the flow due to its height and shape. Consequently, the streamlines bypass the obstacle leading to a curved shear layer that reattaches downstream. Thus, the vortices shed at separation are convected toward the wall, where injection has the effect of vorticity amplification. This mechanism is attributed by some authors to the longitudinal pressure gradient effect along the injecting wall.^{25,26}

Downstream the reattachment length, the vortices develop as wall vortices, as observed without the obstacle.²⁷ Therefore, flow development is characterized not by two instabilities but by only one, which combines the characteristics of the shear layer and the wall vortex shedding. Moreover, in this mechanism, frequency jumps are not induced by a vortex-pairing phenomenon but rather result from a modification in the number of vortices developing between separation and impingement,²⁸ as is usually considered.²⁹ This mechanism may be, consequently, responsible for the characteristic behavior observed in test case 3. On the contrary, two vortex-shedding phenomena seem to develop for test case 2. Wall velocity spectra show the development of wall vortices; due to the relatively small height of the obstacle, the records of velocity fluctuations close to the injecting wall show frequency shifts. These frequency shifts are not representative of the wall velocity fluctuations but rather arise from the induced field generated by the vortices convecting from the top of the obstacle. In fact, the straight obstacle induces the development of a shear layer instability whose oscillations are driven by pressure fluctuations through a coupling phenomenon. Furthermore, it can be seen that, for the highest Mach numbers, wall vortex development

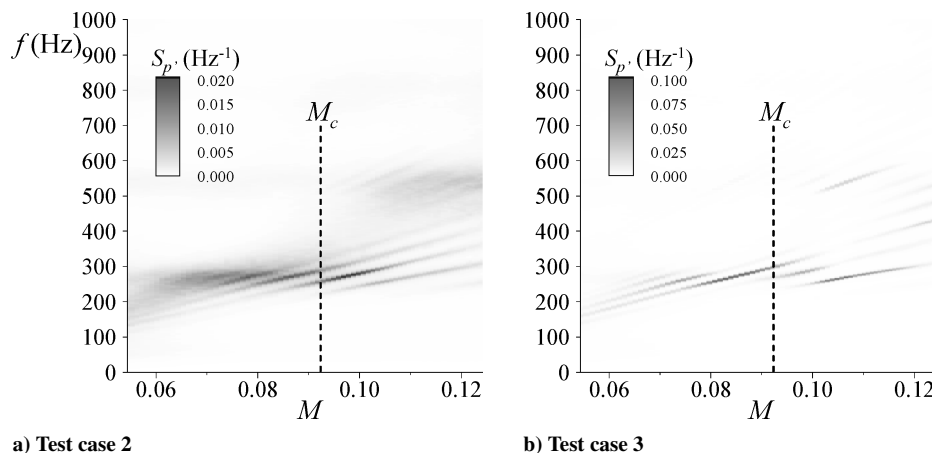


Fig. 6 Pressure spectra of cold-gas simulations of test cases 2 and 3 for $H_c = H_1$.

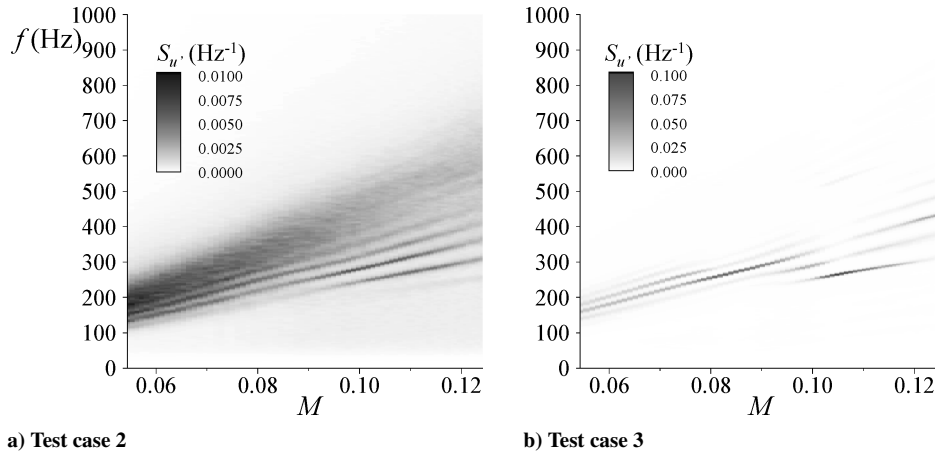


Fig. 7 Wall velocity spectra of cold-gas simulations of test cases 2 and 3 for $H_c = H_1$.

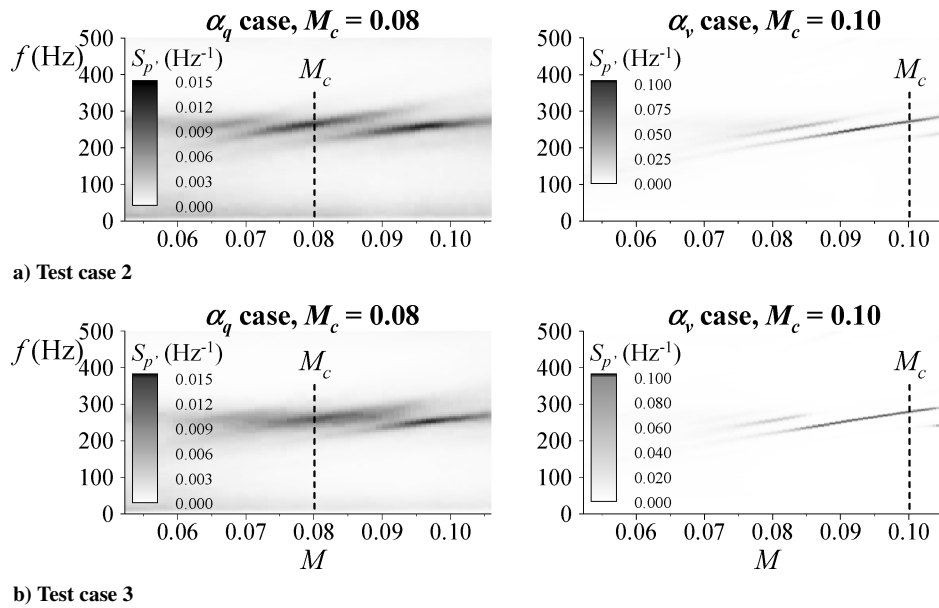


Fig. 8 Pressure spectra of cold-gas simulations of test cases 2 and 3 for $H_c = H_2$.

induces excitation of the second acoustic mode leading to the disappearance of the coupling. Then the wall instability appears as the main instability in the flowfield. Some numerical aspects of these phenomena are developed in Ref. 30, and the numerical simulations of test cases 2 and 3 may be found in Ref. 31.

The cold-gas simulations for $H_c = H_2$ are presented in Fig. 8. For α_q , pressure oscillation behavior is similar in the two test cases. The increase of the Mach number shows two main shifts of the f_1 frequency, the first one arising around the characteristic Mach number $M_c = 0.08$. When the injection velocity ratio is taken into account (α_v case), no main differences from the two test cases appear. Pressure oscillations are particularly organized on discrete frequencies characteristic of a shear layer instability reinforced in vorticity by the injecting wall.²⁴ Once again, a frequency shift is present around $M_c = 0.1$. By the comparison with the results obtained from the firing tests of Fig. 2, satisfactory agreement is observed because the two test cases show a high level of oscillations on the first acoustic mode.

From a qualitative point of view, it appears that the α_q and α_v cases are in a position to predict the flow organization of firing tests. Table 2 gives the f_1 amplitude for the overall simulations. The results of firing tests show that, at $t = t_2$, the levels have the same order of magnitude for the two test cases, with a lower value obtained at $t = t_1$ for test case 3. For cold-gas simulations, the ratio α_q cannot predict this trend. In fact, the unbalanced mass flow rate has two

Table 2 Nondimensional fluctuating pressure levels of f_1 mode, %

		Cold-gas simulations	
t	Combustors	α_q case	α_v case
<i>Test case 2</i>			
t_2	0.123	0.007	0.044
<i>Test case 3</i>			
t_1	0.095	0.031	0.031
t_2	0.118	0.007	0.063

main effects. First, the increase of the second injecting block mass flow rate induces high-velocity fluctuations when impinging on the obstacle, as shown previously.¹⁹ Second, the decrease of the third injecting block mass flow rate implies a decrease of the injection Reynolds number, which increases the turbulence development.⁸ The resulting fluctuating flowfield shows a decrease of the vortex coherence and favors the occurrence of random fluctuations, leading to a small noise level. However, when the α_v ratio is considered, the order of magnitude between the different simulations is more similar to the firing test results with the lowest level obtained at $t = t_1$. These observations show that the best quantitative description of the firing tests is obtained with α_v .

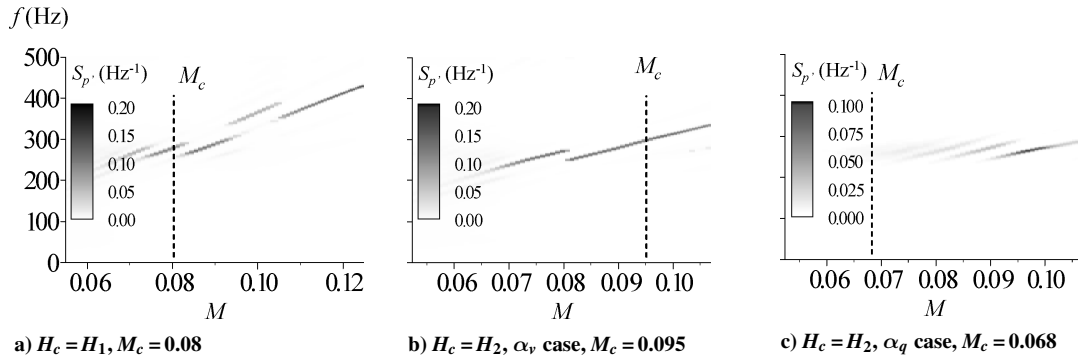


Fig. 9 Pressure spectra of cold-gas simulations of test case 4.

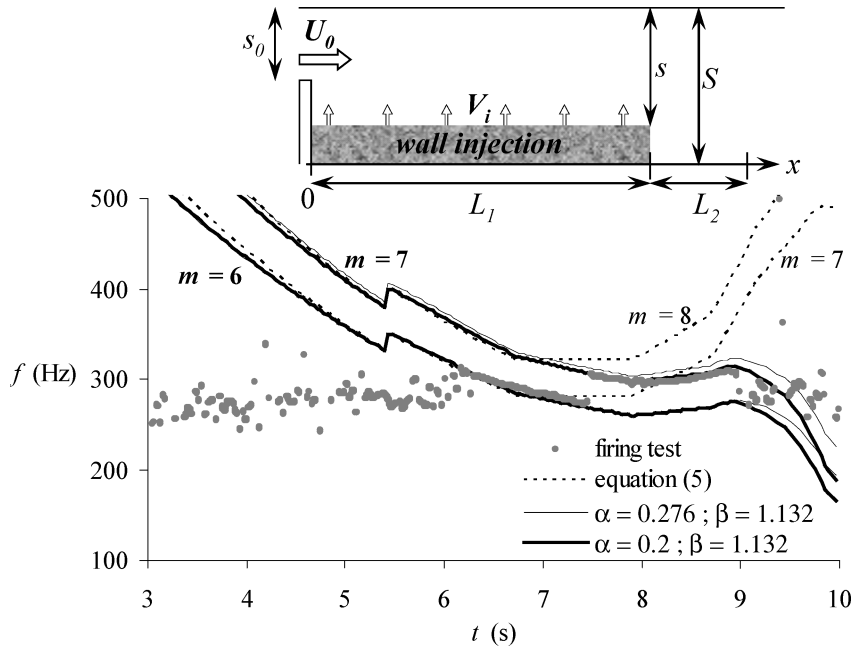


Fig. 10 First acoustic mode evolution for test case 4.

C. Test Case 4

The cold-gas simulations of test case 4 are presented in Fig. 9. Whatever the channel height and the α_v or α_q ratio, the presence of discrete frequencies associated with shifts depending on the Mach number shows the development of a strong coupling phenomenon inside the flow. The height of the obstacle is 1 mm for $H_c = H_1$ and reaches 6 mm for $H_c = H_2$. Under these conditions, the obstacle presents a relatively small perturbation for the flow where the instability initiated at the top of the obstacle is amplified by vorticity generation at the injecting wall. The characteristic Mach number $M_c = 0.08$ is located on a frequency shift for $H_c = H_1$ as well as for $M_c = 0.095$ when the α_v ratio is taken into account for $H_c = H_2$. However, by the considering of the α_q ratio, the level of M_c is not high enough to reach the first frequency shift of the coupling mechanism, whereas strong pressure oscillations are observed for the firing test (cf., Fig. 2). The conclusion of the preceding section is then confirmed here from a qualitative point of view: The prediction of firing tests by cold-gas simulations must be undertaken using the conservation of the ratio between the injection velocities. Thus, it appears that the Mach number scaling at the inhibitor section is justified a posteriori. The Strouhal similitude refers to the shear layer, whereas most of the test cases show the development of wall vortices. Nevertheless, in view of the relatively satisfactory good agreement between small-scale motor results and cold-gas simulations, the most important phenomenon implying high levels of pressure oscillations is the mechanism where the shear layer instability is reinforced by vorticity generation at the injecting wall. The α_v ratio allows the timescale to be properly simulated based on the injection velocity, whose the surface mechanism is dependent.

The aim of the study was to characterize the frequency shifts in the acoustic mode behavior. To explain the resonant frequency evolution during the combustion of solid rocket motors, Rossiter's analysis²⁸ is customarily used. It is based on the hypothesis that a coupling phenomenon is described by the fact that the vortex structures are the sources of their own shedding. Under these conditions, if m is the number of vortices located between separation and impingement, and T is the oscillation period, by taking into account the two branches of the self-sustained loop the following expression for the total duration of one cycle of the phenomenon is obtained:

$$mT = L/U_c + L/a \quad (4)$$

where L is the separation to impingement distance, that is, between the inhibitor and the nozzle, and a is the speed of sound. The oscillation frequency $f = 1/T$ can then be written

$$f = (am/L)[1/(1 + a/U_c)] \quad (5)$$

To obtain the value of the frequency, it is necessary to estimate the velocity U_c at which the vortices travel. Usually, the convection velocity is expressed as the product of a convection coefficient k with the velocity in the section of the flow at separation, as is done for jet instabilities.^{32,33} In the cases of ramjet and cavity studies, Dotson et al.²⁹ cited values between 0.5 and 0.6 and retained a value of 0.58.

Test case 4 was taken as an example to estimate the validity of Eq. (5). Figure 10 presents the evolution of the first acoustic mode frequency with the combustion time. This evolution is mainly characterized, for $t > 6$ s, by two shifts of the frequency separated by

a frequency jump at $t = 7.5$ s. Two curves added in Fig. 10 have been obtained from Eq. (5) with $m = 7$ and $m = 8$ and using $k = 0.58$. As can be seen, poor agreement is observed between the theory and the firing results. Particularly, in the range $6.7 < t < 8$ s, the theoretical frequency is constant. Indeed, at $t = 6.7$ s, the propellant height reaches the top location of the inhibitor, implying a constant area at the inhibitor section for larger combustion times and, thus, a constant convection velocity.

Several points may be discussed as regard this latter result. The first one involves the initial hypothesis. Indeed, convection velocity is supposed to be proportional to the mean velocity in the inhibitor section, but downstream this position, the gas production generated by the combustion of the aft segment induces an acceleration of the flow. Then, it is probable that the velocity at which the vortices travel is increased, and this effect is not taken into account in the present investigation. Furthermore, the conicity of the aft segment implies a decrease of its length after $t = 8$ s, and this may also affect convection velocity.

However, previous studies on pressure oscillations occurring in solid propellant motors involved different configurations compared with the present small-scale motors. In most of the cold-gas simulations dealing with vortex convection velocities, the combustion of propellant is not simulated, that is, no wall injection occurs, as in the studies of cylindrical cavities with baffles to represent inhibitors.⁴ On the other hand, in the analyses of pressure oscillation data of rocket motors, the configurations do not have inhibitors. Therefore, the velocity estimated in the inhibitor section evolves during the combustion and intrinsically takes into account the effects induced by the presence of an injection velocity accelerating the convection velocity.²⁹ For these reasons, no model dealing with both the presence of a section restriction due to the presence of an inhibitor and the wall injection exists.

The use of cold-gas simulations can, therefore, be dedicated to this approach. As a result of the calculation of spatiotemporal cross-correlation coefficients,¹⁹ a convection velocity has been estimated for each of the channel heights in the simulation of test case 4. For $H_c = H_2$, k reaches a value of 0.587, close to the previous value taken according to the results of Dotson et al.²⁹ For $H_c = H_1$, the value is close to 0.55, whereas the cross section at the inhibitor location is the same. These results, therefore, show that convection velocity may be sensitive to another parameter. The aim is to propose a model for estimating U_c that takes into account the injection velocity downstream from the obstacle location.

A schematic of the configuration studied is added in Fig. 10. A flow of velocity U_0 generated in a section s_0 develops in a duct of section s and length L_1 fed by a wall injection of velocity V_i . Then the flow takes place in a duct of section S and length L_2 without injection. The mean velocity $U(x)$ in each section for $0 < x < L_1$ is

$$U(x) = U_0(s_0/s) + V_i(w/s)x \quad (6)$$

where w is the injecting channel section perimeter at the location x . The second term of this equation represents the increase of the mean velocity due to the injection velocity. The proposed model assumes that the local convection velocity U_c is simultaneously proportional to the velocity U_0 and the increase in the mean velocity,

$$U_c(x) = \alpha U_0 + \beta V_i(w/s)x \quad (7)$$

where α and β are constants. By integration, the mean convection velocity $\overline{U_c}$ between $x = 0$ and $x = L_1$ is deduced from the mean convection time T_1 ,

$$T_1 = L_1/\overline{U_c} = (s/\beta w V_i) \ln[1 + (\beta/\alpha)(V_i/U_0)(wL_1/s)] \quad (8)$$

The length L_2 (cf., Fig. 10) represents the aft end of a solid rocket motor where the propellant is completely burnt. For $L_1 < x < L_2$, the convection velocity is assumed to be constant and equal to $U_c(L_1)$. However, in reality, the propellant thickness gradually decreases until $x = L_1$. To take into account the change of section at $x = L_1$,

the mean convection time T_2 between $x = L_1$ and $x = L_2$ is assumed to be

$$T_2 = [L_2/U_c(L_1)](s/S) \quad (9)$$

In cold-gas simulations, the time T_2 is equal to zero, and the injection velocity is proportional to U_0 , so that according to Eq. (8), $\overline{U_c}$ is proportional to V_i , that is, M . As already explained, two convection coefficients have been deduced from experimental data obtained for the two channel heights. The constants of the model have then been estimated to be

$$\alpha = 0.276, \quad \beta = 1.132 \quad (10)$$

Then, the model was applied to the estimated geometric and dynamic data of test case 4. Figure 10 shows the results obtained using Eqs. (8) and (9) in Eq. (4). Even if the model does not exactly fit the firing test results, an improvement may be observed. The first frequency shift is close to the model with $m = 6$ vortices.

Less satisfactory agreement is obtained with the second shift, $m = 7$, but the general trends of the first mode evolution are clearly reproduced, that is, a decrease, then an increase, and a new decrease of the oscillation frequency. When constant α is adjusted to 0.2, it is observed that more accurate prediction of the frequency evolution is obtained. In fact, because of the measurements accuracy and the relatively close values of the convection coefficients obtained for the two channel heights, it appears that the values of α and β are highly sensitive to the experimental results. This indicates that the model may be improved to better reproduce the firing tests.

IV. Conclusions

The aim of the study was to analyze the pressure oscillation behavior occurring during firing tests of small solid rocket motors by means of a cold-flow setup. Four configurations, with similar propellant segments, were retained involving different inhibitor shapes and protrusions in the flow. Cold-gas simulations for two combustion times, corresponding to two channel heights, have been defined from the time history data of pressure oscillations. For the dynamic conditions, the similitude is based on the mean Mach number at the inhibitor ring. Moreover, two boundary conditions were considered, conserving either the ratio of the injection velocities of the two segments or the ratio of the mass flow rates.

A general agreement is observed between the firing tests and the simulations. Some general trends have been described for the first firing test case that allowed one to analyze a transition mechanism from a given mode to an inferior one despite the increase of the internal Mach number. A restrictor with a strong protrusion actually generates high random velocity fluctuations leading to weak receptivity of wall velocity fluctuations to pressure oscillations, and therefore, no strong instability is observed. Comparisons between cold-gas simulations of tests involving different shapes for the same height (test cases 2 and 3) show that simple bending of the restrictor modifies the unsteady behavior arising from the natural or forced nature of the flowfield oscillations. More specifically, the curved obstacle allows for a stronger interaction between the vortices generated at the top of the restrictor and the wall injection, thus, providing a stronger excitation of the first axial mode.

Therefore, the main phenomenon furnishing high vortex-shedding-driven pressure oscillation levels is wall instability when strong coupling with the acoustic is possible. This condition is observed when a short protruding restrictor allows the flow to reattach downstream. The location of the wall vortex formation is in this way imposed close to the middle of the chamber where the amplitude of the acoustic velocity reaches its maximum. Moreover, the bending of the inhibitor also modifies the turbulence development by its geometry as long as the shearing created by the obstacle is likewise modified.

The results obtained show that despite the simple representation of a cold-gas simulation compared with all of the phenomena intrinsically linked to the combustion of the propellant, the instability developments are well described. Therefore, a cold-flow setup represents an easy way for a preliminary technology choice in internal design of a solid rocket motor chamber. As far as the pressure

oscillation reduction is concerned, studies involving different injection velocities between the segments or focusing on different inhibitor shapes may be undertaken. For example, the acoustic response of combustors with unbalanced mass flow rates leading to an increase of the central segment injection velocity could be tested to estimate the quantitative effects on pressure levels. On the other hand, influence of slots in the axisymmetric inhibitor could perturb the instability development by three-dimensional effects and could be easily investigated by cold-flow simulations.

Acknowledgments

This work has been supported by the Centre National d'Etudes Spatiales concerning the study of the instabilities of the MPS/P230 of Ariane 5. The authors give special thanks to Michel Pons, director of the Solid Propulsion Department, for his tireless aid and are particularly grateful to Mauro Augelli for his continuing support on this project.

References

- ¹Hourigan, K., Welsh, M. C., Thompson, M. C., and Stokes, A. N., "Aerodynamic Sources of Acoustic Resonance in a Duct with Baffles," *Journal of Fluids and Structures*, Vol. 4, 1990, pp. 345–370.
- ²Dunlap, R., and Brown, R. S., "Exploratory Experiments on Acoustic Oscillations Driven by Periodic Vortex Shedding," *AIAA Journal*, Vol. 19, No. 3, 1981, pp. 408, 409.
- ³Culick, F. E. C., and Magiawala, K., "Excitation of Acoustic Modes in a Chamber by Vortex-Shedding," *Journal of Sound and Vibration*, Vol. 64, No. 3, 1979, pp. 455–457.
- ⁴Flatau, A., and Van Moorhem, W. K., "Prediction of Vortex Shedding Responses in Segmented Solid Rocket Motors," AIAA Paper 90-2073, July 1990.
- ⁵Rockwell, D., and Naudasher, E., "Self-Sustained Oscillations of Impinging Free Shear Layers," *Annual Review of Fluid Mechanics*, No. 71, 1979, pp. 67–94.
- ⁶Rockwell, D., "Oscillations of Impinging Shear Layers," *AIAA Journal*, Vol. 21, No. 5, 1983, pp. 645–664.
- ⁷Traineau, J. C., Hervat, P., and Kuentzmann, P., "Cold-Flow Simulation of a Two-Dimensional Nozzleless Solid Rocket Motor," AIAA Paper 86-1447, June 1986.
- ⁸Beddini, A. R., "Analysis of Injection Induced Flows in Porous Walled Duct with Application to Aerochemistry of Solid Propellant Motor," Ph.D. Dissertation, Dept. of Mechanical and Aerospace Engineering, Rutgers Univ., New Brunswick, NJ, Oct. 1981.
- ⁹Yeh, Y. P., Heaman, J. P., Ramachandran, N., and Smith, A. W., "Subscale Cold Flow Simulation of the Port Flow in Solid Rocket Motors," AIAA Paper 94-3294, June 1994.
- ¹⁰Dunlap, R., Blackner, A. M., Waugh, R. C., Brown, R. S., and Willoughby, P. G., "Internal Flowfield Studies in a Simulated Cylindrical Port Rocket Chamber," *Journal of Propulsion and Power*, Vol. 6, No. 6, 1990, pp. 690–704.
- ¹¹Shu, P. H., Sforzini, R. H., and Foster, W. A., "Vortex-Shedding from Solid Rocket Propellant Inhibitors," AIAA Paper 86-1418, June 1986.
- ¹²Menon, S., and Jou, W. H., "Numerical Simulations of Oscillatory Cold Flows in an Axisymmetric Ramjet Combustor," *Journal of Propulsion and Power*, Vol. 6, No. 5, 1990, pp. 525–534.
- ¹³Lupoglazoff, N., and Vuillot, F., "Numerical Simulations of Parietal Vortex-Shedding Phenomenon in a Cold Flow Set-Up," AIAA Paper 98-3220, July 1998.
- ¹⁴Najjar, F. M., Ferry, J., Wasistho, B., and Balachandar, S., "Full-Physics Large-Scale Multiphase Large Eddy Simulations of Flow inside Solid Rocket Motors," AIAA Paper 2002-4343, July 2002.
- ¹⁵Apte, S. V., and Yang, V., "A Large-Eddy Simulation Study of Transition and Flow Instability in a Porous-Walled Chamber with Mass Injection," *Journal of Fluid Mechanics*, Vol. 477, 2003, pp. 215–225.
- ¹⁶Le Breton, P., Ribéreau, D., and Godfroy, F., "SRM Performance Analysis by Coupling Bidimensional Surface Burnback and Pressure Field Computations," AIAA Paper 98-3968, July 1998.
- ¹⁷Traineau, J. C., Prévost, M., Vuillot, F., Le Breton, P., Cuny, J., Preioni, N., and Bec, R., "A Subscale Test Program to Assess the Vortex Shedding Driven Instabilities in Segmented Solid Rocket Motors," AIAA Paper 97-3247, July 1997.
- ¹⁸Vétel, J., Plourde, F., and Doan-Kim, S., "Mixing Effects Between Self-Sustained Oscillations and Unstable Hydrodynamic Behavior near Injecting Walls," *AIAA Journal*, Vol. 39, No. 8, 2001, pp. 1455–1468.
- ¹⁹Vétel, J., Plourde, F., and Doan-Kim, S., "Dynamics of an Internal Flowfield Driven by Two Hydrodynamic Instabilities," *AIAA Journal*, Vol. 41, No. 3, 2003, pp. 424–435.
- ²⁰Godon, J. C., "Code Perse: Une Approche Unidimensionnelle dans la Modélisation du Fonctionnement Stationnaire d'un Propulseur à Propergol Solide," *Colloque R&T, Ecole Nationale Supérieure de Mécanique et d'Aérotechnique Poitiers, France*, March 1998.
- ²¹Flandro, G. A., "Vortex Driven Mechanism in Oscillatory Rocket Flows," *Journal of Propulsion and Power*, Vol. 2, No. 3, 1986, pp. 206–214.
- ²²Wu, W. J., and Kung, L. C., "Determination of Triggering Condition of Vortex-Driven Acoustic Combustion Instability in Rocket Motors," *Journal of Propulsion and Power*, Vol. 16, No. 6, 2000, pp. 1022–1029.
- ²³Vétel, J., Plourde, F., and Doan-Kim, S., "Characterization of a Coupled Phenomenon in a Confined Shear-Layer," *International Journal of Heat and Fluid Flow*, Vol. 23, No. 4, 2002, pp. 533–543.
- ²⁴Vétel, J., Plourde, F., and Doan-Kim, S., "Amplification of a Shear-Layer Instability by Vorticity Generation at an Injecting Wall," *AIAA Journal*, Vol. 42, No. 1, 2004, pp. 35–46.
- ²⁵Majdalani, J., and Van Moorhem, W. K., "Multiple-Scales Solution to the Acoustic Boundary Layer in Solid Rocket Motors," *Journal of Propulsion and Power*, Vol. 13, No. 2, 1997, pp. 186–193.
- ²⁶Kirkkopru, K., Kassoy, D. R., and Zhao, Q., "Unsteady Vorticity Generation and Evolution in a Model of a Solid Rocket Motor," *Journal of Propulsion and Power*, Vol. 12, No. 4, 1996, pp. 646–654.
- ²⁷Vétel, J., Plourde, F., and Doan-Kim, S., "Analysis of Self-Sustained Oscillation Sources in Segmented Flows," *Experiments in Fluids*, Vol. 33, 2002, pp. 516–530.
- ²⁸Rossiter, J. E., "Wind-tunnel Experiments on the Flow Over Rectangular Cavities at Subsonic and Transonic Speeds," Aeronautical Research Council, Ministry of Aviation, Reports and Memoranda 3438, London, Oct. 1964.
- ²⁹Dotson, K. W., Koshigoe, S., and Pace, K. K., "Vortex Shedding in a Large Solid Rocket Motor Without Inhibitors at the Segment Interfaces," *Journal of Propulsion and Power*, Vol. 13, No. 2, 1997, pp. 197–206.
- ³⁰Vétel, J., Plourde, F., Doan-Kim, S., and Guéry, J.-F., "Numerical Simulations of Wall and Shear-Layer Instabilities in Cold Flow Setup," *Journal of Propulsion and Power*, Vol. 15, No. 2, 2003, pp. 297–306.
- ³¹Le Breton, P., Guéry, J. F., Vuillot, F., and Prevost, M., "Recent Advances in the Prediction of SRM Thrust Oscillations," 1^{er} Colloque Européen sur la Technologie des Lanceurs, Centre National d'Etudes Spatiales, Dec. 1999.
- ³²Oler, J. W., and Goldschmidt, V. W., "Coherent Structures in the Similarity Region of Two-dimensional Turbulent Jets," *Journal of Fluids Engineering*, Vol. 106, 1984, pp. 187–192.
- ³³Ho, C. M., and Nosseir, N. S., "Dynamics of an Impinging Jet. Part 1: the Feedback Phenomenon," *Journal of Fluid Mechanics*, Vol. 105, 1981, pp. 119–142.